Nonisometric Surface Registration via Conformal Laplace-Beltrami Basis Pursuit

Stefan C. Schonsheck · Michael M. Bronstein · Rongjie Lai

Received: date / Accepted: date

Abstract Surface registration is one of the most fundamental problems in geometry processing. Many approaches have been developed to tackle this problem in cases where the surfaces are nearly isometric. However, it is much more challenging to compute correspondence between surfaces which are intrinsically less similar. In this paper, we propose a variational model to align the Laplace-Beltrami (LB) eigensytems of two non-isometric genus zero shapes via conformal deformations. This method enables us to compute geometrically meaningful point-to-point maps between non-isometric shapes. Our model is based on a novel basis pursuit scheme whereby we simultaneously compute a conformal deformation of a 'target shape' and its deformed LB eigensystem. We solve the model using a proximal alternating minimization algorithm hybridized with the augmented Lagrangian method which produces accurate correspondences given only a few landmark points. We also propose a re-initialization scheme to overcome some of the difficulties caused by the non-convexity of the variational problem. Intensive numerical experiments illustrate the effectiveness and robustness of the proposed method to handle non-isometric surfaces with large deformation with respect to both noises on the underlying manifolds and errors within the given landmarks or feature functions.

 $\textbf{Keywords} \ \, \textbf{Shape Analysis} \cdot \textbf{Laplace-Beltrami eigensystem} \cdot \textbf{Conformal Deformation} \cdot \textbf{Nonisometric manifold matching}$

1 Introduction

The computation of meaningful point-to-point mappings between pairs of manifolds lies at the heart of many shape analysis tasks. It is crucial to have robust methods to compute dense correspondences between two or more shapes in different applications including shape matching, label transfer, animation and recognition [17, 24, 32, 36, 45, 50]. In cases where shapes are very similar (isometric or nearly isometric), there are many approaches for computing such correspondences [3, 9, 13, 15, 21, 22, 26, 32, 43, 44]. However, it is still challenging to compute accurate correspondences when the deformation between the shapes are far away from near isometry.

One of the key challenges in largely deformed non-isometric shape matching is that the intrinsic features of the two shapes are not similar enough for standard techniques to recognize their similarity. For example, when computing the correspondence between human faces, it is not particularly difficult to geometrically

Department of Mathematics, Rensselaer Polytechnic Institute, Troy, NY 12180, U.S.A.

E-mail: schon@rpi.edu

M. Bronstein

Department of Computing, Imperial College London, London, U.K.

E-mail: m.bronstein@imperial.ac.uk

R Lai

Department of Mathematics, Rensselaer Polytechnic Institute, Troy, NY 12180, U.S.A.

E-mail: lair@rpi.edu

S. Schonsheck

characterize the structure of a 'nose'. However, similar techniques can not work well to compute a map between a horse and an elephant face since these two surfaces have many largely deformed local structures including the drastic difference between the trunk of the elephant and the nose of the horse. Because of this, it is crucial to develop new methods to adaptively characterize large deformations on surfaces.

The LB eigensystem is a ubiquitous tool for 3D shape analysis (see [3, 6, 10, 27, 28, 30, 34, 36, 38, 41, 42, 43, 47] and references therein). It is invariant under isometric transformations and intrinsically characterizes the local and global geometry of manifolds through its eigensystem up to an isometry. In principle, the LB eigensystem reduces high-dimensional nonlinear isomorphism ambiguities between two isometric shapes to a linear transformation group between two LB eigensystems. This linear transform is necessary due to the possible sign or sub-eigenspace (geometric multiplicity) ambiguity of LB eigensystems [26]. Additionally, similar shapes often have similar eigensystems which allow for joint analysis of similar shapes their spectral properties [32]. However, when the deformation between two shapes is far from an isometry, the large dissimilarity between LB eigensystems of two shapes is the major bottleneck to adapt the existing spectral geometry approach to conduct registration.

A natural idea to extend spectral geometry methods to register non-isometric surfaces is to deform the metric of a "target surface" to the metric of a "source surface" so that two surfaces share similar LB eigensystems after deformation. However, directly computing this deformation often requires specific knowledge about corresponding regions of the surfaces. In this work, we propose a method to simultaneously compute such a deformation while learning features that can be used for registration. Mathematically, one way to characterize this type of deformation is through measuring its conformal factor—the local scaling induced by a conformal deformation. It is well known that there exists a conformal mapping between any two genus-zero surfaces [19]. Rather than reconstruct the conformally deformed surfaces and/or exact conformal map, we exploit a fundamental link between the conformal factor and the LB eigensystem by manipulating the conformally deformed LB eigensystem. This allows us to compute a new basis on the target surface to align the naturally defined LB eigensystem on the source surface. This leads to a variational method for non-isometric shape matching which enables us to overcome the natural ambiguities of the LB eigensystem and align the bases of non-isometric shapes while avoiding the direct computation of conformal maps.

Numerically, we solve our model using a proximal alternating minimization (PAM) method [1] hybridized with the augmented Lagrangian method [14]. The method is iteratively composed of a curvilinear search method on orthogonality constrained manifold [54] in one direction to compute the conformally deformed LB eigenfunctions and the BFGS [5] method for the other direction to compute the conformal factor. Theoretically, we guarantee the local convergence of the proposed algorithm since the objective function and constraints satisfy the necessary Kurdyka-Lojasiewicz (KL) condition [1]. Comprehensive numerical results on largely deformed problems, including horse-to-elephant and Faust benchmark database [7], validate the effectiveness and robustness of our method.

Related Works. A large number of 3D nonrigid shape matching approaches are based on analysis of the LB eigensystem (see [10, 22, 26, 30, 32, 33, 35, 36, 38, 43] and reference therein). The LB eigensystem is intrinsic and invariant to isomorphism, and also characterizes the local and global geometry of a manifold. This makes it ideal for many shape processing tasks and many early works in the field involve directly comparing the LB spectrum of the shapes to determine how alike shapes are [30, 35, 36]. More recently, the general concept of functional maps [32] has played a central role in many new methods that have allowed for the formulation of accurate correspondence maps. This technique essentially reduces the non-linear transform between two shapes to a linear transform between their eigensystems. In general, these techniques work well for isometric and near isometric cases, but can not produce satisfactory results when the LB eigensystems of shapes are very dissimilar. This occurs when the deformation between shapes is far from an isometry. To overcome this, the concept of coupled bases (also known as joint-diagonalization) was introduced for shape processing tasks in [22]. In this work, the authors propose a variational model to define a shared basis for a pair of shapes which is 'nearly harmonic' on one shape and 'similar' to the natural LB basis on the other. This joint optimization allows for much more accurate correspondence, but does not characterize the underlying deformations which lie at the heart of the non-isometric shape matching problem.

Conformal maps have been widely applied to various shape processing tasks in order to characterize surface deformations [15, 16, 18, 46]. In one of the first works to combine spectral and deformation based approaches, [40] presents a scheme to find optimal conformal deformation to align two shapes in the em-

bedded LB Space. Additionally, the authors present a general framework for computing LB eigensystems of conformally deformed surfaces as well as several other imported related quantities. Continuing on this line of work in [20], the authors use the LB eigenvalues as a tool to guide conformal deformations. Using derivatives of the LB eigenvalues, they compute optimal conformal metrics which approximate conformal and topological eigenvalues. In our work, we use the spectral coefficients of known features to guide the deformation, so rather than align the eigenvalues we align the eigenfunctions. This allows us to avoid the subspace ambiguity of the LB eigensystem and computational errors in calculating high-frequency eigenvalues.

Major Contributions. We introduce a novel variational basis pursuit model for computing non-isometric shape correspondences via a conformal deformation of the LB eigensystem. This model enhances spectral approaches from handling nearly isometric surface registration to tackling surfaces with large deformed metrics. It naturally combines the conformal deformation to the LB eigensystem and simultaneously computes surface deformations and LB eigenbasis which also automatically overcomes the ambiguities of LB eigensystems in surface registration. We also propose a numerical scheme to solve the variational model with a local convergence guarantee. Additionally, we introduce a reinitialization scheme to help tackle local minima and improve the quality of the computed bases. This algorithm successfully handles non-isomorphic shape correspondence problems given only a few landmarks and is shown to be robust to noise and perturbations of landmarks.

The rest of this work is organized as follows: In section 2, we review the theoretical background of conformal deformations of LB eigensystem and functional maps. After that, we propose the variational basis pursuit model for conformal deformations of the LB eigensystem in section 3. In section 4, we discretize the model and develop an optimization scheme based on PAM to solve the variational problem. Section 5 is further devoted to discussing a few details of the model and a reinitialization scheme to improve our numerical solver. In section 6, numerical results on several data sets are presented to show that the model accurately produces point-to-point mappings on non-isometric manifolds with large deformation given only a few landmark points. We also show that our approach is robust to both noises in the underlying manifolds and inaccuracies in the initial landmarks. Furthermore, we test the model to a benchmark data based to show its effectiveness. Lastly, we conclude our discussions of this project in Section 7.

2 Mathematical Background of LBBP

In this section, we discuss the mathematical background of the proposed method. We first review a few key properties of the LB eigensystem of a Riemannian surface and discuss its conformal deformations with respect to deformations of the Riemannian surface metric [11, 19]. After this, we review the functional maps framework in [32] which will be closely related to our work.

2.1 Conformal Deformation of LB Eeigensystem on Riemannian Surfaces

Given a closed Riemannian surface (\mathcal{M}, g) , its LB operator in a given local coordinate system, $\{x_i\}_{i=1,2}$, is defined as [11, 19]:

$$\Delta_g \phi = \frac{1}{\sqrt{G}} \sum_{i=1}^2 \frac{\partial}{\partial x_i} (\sqrt{G} \sum_{i=1}^2 g^{ij} \frac{\partial \phi}{\partial x_j}) \tag{1}$$

where (g^{ij}) is the inverse of the metric matrix $g=(g_{ij})$ and $G=\det(g_{ij})$. The LB operator is self-adjoint and elliptic, therefore it has a discrete spectrum. We denote the eigenvalues of $-\Delta_g$ as $0=\lambda_0<\lambda_1\leq\lambda_2\leq\cdots$ with the corresponding eigenfunctions $\phi_0,\phi_1,\phi_2,\cdots$ satisfying:

$$-\Delta_g(x)\phi_i(x) = \lambda_i\phi_i(x), \quad \text{and} \quad \int_{\mathcal{M}} \phi_i(x)\phi_j(x) \, dvol_g(x) = \delta_{ij}, \quad i, j = 0, 1, 2, \cdots$$
 (2)

where $dvol_g(x)$ is the area element on \mathcal{M} with respect to g. It is well-known that $\Phi = \{\phi_n \mid n = 0, 1, 2, \cdots\}$ forms an orthonormal basis for the real-valued, smooth function space $C^{\infty}(\mathcal{M}, \mathbb{R})$ on the manifold (\mathcal{M}, g) . This basis can be viewed as a generalization of the Fourier basis from flat space to a differentiable manifold.

The LB eigensystem is invariant under both rigid and nonrigid isometric transformations, and it uniquely determines a manifold up to isometry [6].

In differential geometry, a conformal map is one which preserves angles locally. Formally, a conformal map preserves the first fundamental form up to a positive scaling factor. Given two manifolds (\mathcal{M}_1, g_1) and (\mathcal{M}_2, g_2) , a map $F: (\mathcal{M}_1, g_1) \to (\mathcal{M}_2, g_2)$ is conformal if and only if the pullback $F^*(g_2) = w^2 g_1$ with a positive function w^2 (written this way to emphasize positivity). A conformal deformation of a surface is a transformation which changes the local metric by a positive scaling factor. A well-known result in conformal geometry is that there exists a conformal map between any two genus-zero surfaces [19].

Given a closed surface (\mathcal{M}, g) with conformal deformation w^2 , the LB eigensystem of the deformed manifold (\mathcal{M}, w^2g) can be viewed as a weighted LB eigensystem on the original surface (\mathcal{M}, g) . This simple fact intrinsically links the LB eigensystem of the deformed manifold to a weighted LB eigensystem on the original manifold. It allows us to compute the LB eigensystem of the conformally deformed manifold without explicitly reconstructing its embedding or coordinates. This also bridges information about the local deformation and global eigensystem, which later becomes the cornerstone of our approach. Formally, we have:

Proposition 1 Let $\{\phi_n^{w^2}, \lambda_n^{w^2}\}_{n=1}^{\infty}$ be a LB eigensystem of a conformally deformed surface (\mathcal{M}, w^2g) , then $\{\phi_n^{w^2}, \lambda_n^{w^2}\}_{n=1}^{\infty}$ is equivalent to the following weighted LB eigensystem on (\mathcal{M}, g) :

$$-\Delta_g \phi_i(x) = \lambda w^2(x)\phi_i(x), \qquad \int_{\mathcal{M}} \phi_i(x)\phi_j(x)w^2(x) \, \mathrm{d}vol_g(x) = \delta_{ij}, \tag{3}$$

Proof This is because:

$$\Delta_{w^2g}\phi = \frac{1}{w^2\sqrt{G}}\sum_{i=1}^2 \frac{\partial}{\partial x_i} (w^2\sqrt{G}\sum_{j=1}^2 w^{-2}g^{ij}\frac{\partial\phi}{\partial x_j}) = w^{-2}\Delta_g\phi$$

Hence the eigen problem: $-\Delta_{w^2g}\phi = \lambda\phi$ is equivalent to $-\Delta_g\phi = \lambda w^2\phi$. Additionally, it is clear that: $\mathrm{d}vol_{w^2g} = w^2\,\mathrm{d}vol_g$, since changing the local metric is equivalent to rescaling the local area element.

The problem of finding the LB eigensystem of a Riemannian manifold is equivalent to finding an orthonormal set of functions $\Phi = \{\phi_i\}$ which have minimal harmonic energy on the surface. From the above proposition, the LB eigensystem of a conformally deformed manifold (\mathcal{M}, w^2g) can be formulated as the following variational problem:

$$\arg\min_{\Phi = \{\phi_i\}} \sum_{i} \int_{\mathcal{M}} ||\nabla_{\mathcal{M}}\phi_i(x)||^2 \, dvol_g(x), \quad \text{s.t.} \quad \int_{M} \phi_i(x)\phi_j(x)w^2(x) \, dvol_g(x) = \delta_{ij}$$
(4)

2.2 Functional Maps

Functional maps were introduced in [32] for isometric and nearly isometric shape correspondence. This method has been shown a very effective tool for various shape processing tasks [22, 32, 37]. Here we provide a basic overview of their framework. Consider Riemannian surfaces (\mathcal{M}_1, g_1) and (\mathcal{M}_2, g_2) , a smooth bijection $F: \mathcal{M}_1 \to \mathcal{M}_2$ induces a linear transformation between functional spaces of these two manifolds as:

$$F_T: C^{\infty}(\mathcal{M}_1, \mathbb{R}) \to C^{\infty}(\mathcal{M}_2, \mathbb{R}), \quad f \mapsto f \circ F^{-1}$$

Instead of computing surface map F, the crucial idea of functional map is to compute the linear map F_T between these two functional spaces. After that, the desired surface map can be encoded by considering images of indicator functions under F_T .

Finding a functional map, F_T , associated with a map F is equivalent to finding the matrix representation of F_T under a fixed orthonormal basis $\{\phi_i\}$ of $C^{\infty}(\mathcal{M}_1, \mathbb{R})$ and a fixed orthonormal basis $\{\psi_i\}$ of $C^{\infty}(\mathcal{M}_2, \mathbb{R})$, respectively. Namely, if we write $F_T(\phi_i) = \sum_j c_{ji}\psi_j$, then any two given corresponding functions $f = \sum_i f_i\phi_i$ and $g = \sum_j g_j\psi_j$ under F_T can be represented using $C = (c_{ij})$ as:

$$F_T(f) = g \Leftrightarrow F_T\left(\sum_i f_i \phi_i\right) = \sum_i f_i F_T(\phi_i) = \sum_i f_i \sum_j c_{ji} \psi_j = \sum_i g_j \psi_j \Leftrightarrow \sum_i c_{ji} f_i = g_j.$$

Each entry of the matrix c_{ij} can be found by finding the j^{th} coefficient of $F_T(\phi_i)$ expressed in the $\{\psi_i\}$ coordinate system, i.e. $c_{ji} = \langle F_T(\phi_i), \psi_j \rangle_{g_2}$. In practice, one can use two finite sets of orthonormal functions to approximate $C^{\infty}(\mathcal{M}_1, \mathbb{R})$ and $C^{\infty}(\mathcal{M}_2, \mathbb{R})$, thus the functional map can be approximated by a finite dimensional matrix. For instance, the first N eigenfunctions of the LB eigensystem is one common choice of such a basis. Then, the problem of finding the transformation F_T can be approximated by the problem of seeking a finite dimension matrix C. As long as C is computed, the desired map F can be computed through C operating on indicator functions.

3 Conformal LB Basis Pursuit for Nonisometric Surface Registration

In this section, we propose a LB basis pursuit model for non-isometric surface registration. On the target surface \mathcal{M}_2 , the model simultaneously finds a conformal deformation and a conformally deformed LB eigensystem so that the coefficients of the corresponding feature functions expressed on the deformed LB eigensystem of \mathcal{M}_2 are the same as the coefficients on the fixed source surface \mathcal{M}_1 .

3.1 Variational PDE model

Given two non-isometric genus-zero Riemannian surfaces (\mathcal{M}_1, g_1) and (\mathcal{M}_2, g_2) , we aim at finding a geometrically meaningful correspondence between these two surfaces. In the case that \mathcal{M}_1 and \mathcal{M}_2 are nearly isometric, there are many successful methods to constructing maps between \mathcal{M}_1 and \mathcal{M}_2 by comparing their isometric invariant features. Using spectral descriptors from solutions of the LB eigensystem on manifolds is a common way of constructing such descriptors [10, 30, 36, 39, 49]. As extensions, some other descriptors such as Heat kernel signature [47], wave kernel signature [3] and optimal spectral descriptors [31] have also been proposed in the literature. However, most of the existing methods consider the construction of descriptors for nearly isometric manifolds. Registration methods based on the existing LB spectral descriptors can not provide satisfactory results for constructing correspondence between two non-isometric surfaces as their eigensystems are possibly quite far apart.

We propose to overcome the limitation of the LB spectral descriptors for largely deformed non-isometric shape registration by considering a continuous deformation of the LB spectral descriptors. Intuitively, given two non-isometric shapes (\mathcal{M}_1, g_1) and (\mathcal{M}_2, g_2) , our idea is to deform the metric of (\mathcal{M}_2, g_2) such that the deformed surface is isometrically the same as (\mathcal{M}_1, g_1) . Then the LB spectral descriptors can be applied as in isometric shape matching. However, it is challenging to find an appropriate deformation as the accurate amount of deformation on each local region of \mathcal{M}_2 depends exactly on an accurate correspondence which is precisely the problem we would like to solve.

To tackle this challenge, we propose to simultaneously find an optimal correspondence and an optimal deformation. More specifically, by fixing the LB eigensystem $\{\Phi, \Lambda\}$ of (\mathcal{M}_1, g_1) , we seek a map $T : \mathcal{M}_1 \to \mathcal{M}_2$ and a conformal factor $w^2 : \mathcal{M}_2 \to \mathbb{R}^+$ such that the LB eigensystem $\{\Phi, \Lambda\}$ of (\mathcal{M}_1, g_1) can be aligned to the LB eigensystem $\{\Psi, \Theta\}$ of $(\mathcal{M}_2, w^2 g_2)$ via T. This problem can be written as the following variational PDE problem:

$$(T^*, w^*, \Psi^*) = \underset{T, w, \Psi = \{\psi_i\}_{i=1}^N}{\arg \min} \sum_{i=1}^N \int_{\mathcal{M}_1} \|\phi_i - \psi_i \circ T\|^2 d\mathcal{M}_1 + \frac{1}{2} \sum_{i=1}^N \int_{\mathcal{M}_2} \|\nabla_{\mathcal{M}_2} \psi_i\|^2 d\mathcal{M}_2,$$

$$\text{s.t.} \quad \int_{\mathcal{M}_2} \psi_i \psi_j \ w^2 d\mathcal{M}_2 = \delta_{ij}$$
(5)

where $d\mathcal{M}_1 = dvol_{g_1}$, $d\mathcal{M}_2 = dvol_{g_2}$ and $w^2d\mathcal{M}_2 = dvol_{w^2g_2}$. The first term measures the alignment of two bases as the correct correspondence should map one LB eigensystem to another one. The second term together with the constraints solves the first N LB eigenfunctions $\{\psi_i\}$ for the deformed manifold (\mathcal{M}_2, w^2g_2) due to the variational problem (4). Existence of a solution to this variational problem (5) is guaranteed as any two genus-0 surfaces are conformally equivalent and the LB operator is invariant under isometric transformations.

Computationally, the numerical search for T in the mapping space is usually very time-consuming. Inspired by the idea of functional maps [32] and the coupled quasi-harmonic bases [22], we choose to represent

T in the functional space. Instead of finding T directly, we look for a basis $\Psi = \psi_i \circ T = F_T(\psi_i)$ which is nearly harmonic on $(\mathcal{M}_2, w^2 g_{\mathcal{M}})$ and represents the corresponding features with the same coefficients as Φ does. More precisely, given a set of corresponding features $F = \{f_1, \cdots, f_k\}$ on \mathcal{M}_1 and $G = \{g_1, \cdots, g_k\}$ on \mathcal{M}_2 , such that $f_i(x) = g_i(y)$ if x and y are corresponding points on \mathcal{M}_1 and \mathcal{M}_2 , we can replace the direct measurement of the basis alignment term with a coefficient matching term. That is, instead of measuring the alignment of Ψ and Φ via T, we measure how closely the coefficients for G in the computed basis Ψ match the coefficients for F in the fixed LB basis Φ . Formally, we measure the coefficient alignment by constructing a matrix of the coefficients in for F in Φ and for G in Ψ so that the ij^{th} term represents the coefficient for the i^{th} corresponding function in the j^{th} basis and computing their difference under the Frobenius norm. With this in mind, we propose the following model:

$$(w^*, \Psi^*) = \underset{w, \Psi}{\arg\min} \frac{r_1}{2} \| \langle F, \Phi \rangle_{g_1} - \langle G, \Psi \rangle_{w^2 g_2} \|_F^2 + \frac{r_2}{2} \sum_{i=1}^N \int_{\mathcal{M}_2} \| \nabla_{\mathcal{M}_2} \psi_i \|^2 d\mathcal{M}_2,$$
s.t.
$$\int_{\mathcal{M}_2} \psi_i \psi_j \ w^2 d\mathcal{M}_2 = \delta_{ij}$$
(6)

where we write:

$$\langle F, \varPhi \rangle_{g_1} = \left(\int_{\mathcal{M}_1} f_i \phi_j \, d\mathcal{M}_1 \right)_{i,j=1,2,\dots,k} \quad \text{and} \quad \langle G, \varPsi \rangle_{w^2 g_2} = \left(\int_{\mathcal{M}_2} g_i \psi_j \, w^2 d\mathcal{M}_2 \right)_{i,j=1,2,\dots,k}.$$

In practice we use indicator functions for F and G, but heat signatures [47], wave kernel signatures [3], or any other corresponding functions will also work. Once $\Psi^* = \{\psi_1^*, \cdots, \psi_{M_2}^*\}$ is obtained, we can easily compute the functional map as

$$F_T: C^{\infty}(\mathcal{M}_1) \to C^{\infty}(\mathcal{M}_2), \qquad F_T(h) = \sum_{i=1} \left(\int_{\mathcal{M}_1} h \phi_i \, \operatorname{d}vol_{g_1} \right) \, \psi_i^{\top}.$$
 (7)

The main advantage of this model over previous existing methods for shape correspondence is that we are able to employ much more of the information encoded in the differential structures of \mathcal{M}_1 and \mathcal{M}_2 in our algorithm by combining the spectral descriptors and local deformations. This additional flexibility enables us to compute correspondences between largely deformed shapes. Information about the conformal deformation of the metric allows us to find a harmonic basis on the deformed shape, meanwhile information about the alignment of the functional spaces guides our calculation of the conformal deformation. Furthermore the additional constraint of the feature alignment overcomes ambiguity casued by the fact that there is no unique conformal deformation between any two genus zero surfaces. To the best of our knowledge, the link between the conformal factor and deformed LB basis has not been exploited in such a way. Previous works have used only the conformal factor [15, 21] or only the functional space [22, 32] as stand alone tools rather than in concert as we present here.

3.2 Regularization and Area Constraint

We add harmonic energy term to smooth the conformal deformation and regularize the problem. This can both increase the speed of the algorithm and improve the quality of the map, both in terms of the geodesic errors of the final correspondence, and the accuracy of the resulting conformal factor. This is particularly helpful to handle deformations between the shapes which are far from isometry and to reduce the required number of features. Rather than smooth the conformal factor w^2 directly, we instead add the harmonic energy of w to the objective function. Using w instead of w^2 allows for easier analytic computation of the derivatives and a more efficient algorithm. In cases where the deformations are likely to be highly localized, this term may be omitted.

Lastly, we add an area preservation constraint to our model. That is, we would like the final deformed shape to be of the same size as the one we are matching it to. To enforce this, we mandate that the deformed

manifold have the same surface area as the original manifold. This eliminates any scaling ambiguity. Then the final version of our model can be stated as:

$$(w^*, \Psi^*) = \underset{w, \Psi = \{\psi_i\}_{i=1}^N}{\min} \frac{r_1}{2} \|\langle F, \Phi \rangle_{g_1} - \langle G, \Psi \rangle_{w^2 g_2} \|_F^2 + \frac{r_2}{2} \sum_{i=1}^N \int_{M_2} \|\nabla_{\mathcal{M}_2} \psi_i\|^2 d\mathcal{M}_2 + \frac{r_3}{2} \int_{\mathcal{M}_2} ||\nabla_{\mathcal{M}_2} w||^2 d\mathcal{M}_2,$$
s.t.
$$\int_{\mathcal{M}_2} \psi_i \psi_j \ w^2 d\mathcal{M}_2 = \delta_{ij} \quad \text{and} \quad Area(\mathcal{M}_1)_{g_1} = Area(\mathcal{M}_2)_{w^2 g_2}$$
(8)

where $Area(\mathcal{M}_1)_{g_1} = \int_{\mathcal{M}_1} 1 d\mathcal{M}_1$ and $Area(\mathcal{M}_2)_{g_2} = \int_{\mathcal{M}_2} w^2 d\mathcal{M}_2$

4 Discretization and Numerical Algorithms

In this section, we describe a discretization of the proposed variational model (8) using on triangular representation of surfaces. After that, we design a numerical algorithm to solve the proposed model based on proximal alternating minimization method.

4.1 Discretization of the LBBP Model

The main method we use to discretize surfaces and differential operators is based on a finite element scheme similar to that developed in [12, 36, 47]. Let $\{p_i\}_{i=1}^n$ be a set of vertices sampled on the manifold \mathcal{M} . A surface can be discretized as a triple $\{P, E, T\}$ made of vertices (P), connected by edges (E) which form triangular faces (T). We define the first ring of p_i , the set of all triangles which contain p_i as $N(p_i)$. For each edge E_{ij} connecting points p_i and p_j , we define the angles opposite E_{ij} as angles α_{ij} and β_{ij} .

We define a diagonal mass matrix, \mathbb{M} , a $n \times n$ positive definite matrix with entries given by:

$$\mathbb{M}_{ii} = \frac{1}{3} \sum_{\tau \in N(p_i)} Area(\tau)$$

We use this simplified version, rather than the standard finite element discretization, for convenience in order to avoid expensive factorizations later in our algorithm. We remark that the standard version can also be used in our algorithm at the cost of speed. The surface area can be approximated as $Area(\mathcal{M}) \approx \sum_{i=1}^{n} \mathbb{M}_{ii}$. Similarly, given a function f on \mathcal{M} with discretization $f: P \to \mathbb{R}$, we have the approximation $\int_{\mathcal{M}} f(x) d\mathcal{M} \approx 1^{\top} \mathbb{M}_{f} = \sum_{i=1}^{n} f_{i} \mathbb{M}_{ii}$. The stiffness matrix, \mathbb{S} , is a $n \times n$ symmetric positive semidefinite matrix given by:

$$\mathbb{S}_{ij} = \sum_{\tau} \int_{\tau} \nabla_{\tau} e_i \cdot \nabla_{\tau} e_j = -\frac{1}{2} [\cot \alpha_{ij}(p_i) + \cot \beta_{ij}(p_i)]$$

where e_i is a linear pyramid function which is 1 at p_i and zero elsewhere. These mass and stiffness matrices can be used to approximate the LB eigenvalue problem as: $\mathbb{S}f = \lambda \mathbb{M}f$.

We remark that one can also work with point clouds representation instead of triangulated meshes. These definitions for the stiffness and mass matrices can be approximated by the point clouds method discussed in [29]. The only change we would need to make is to use only the diagonal entries of the version of the mass matrix M proposed in their paper to populate the strictly diagonal version employed here.

Suppose two surfaces (\mathcal{M}_1, g_1) and (\mathcal{M}_2, g_2) are represented by triangular meshes with the same number of points¹. We denote $\mathbb{M}_1, \mathbb{S}_1 \in \mathbb{R}^{n \times n}$ as the mass and stiffness matrices of \mathcal{M}_1 and let $\Phi \in \mathbb{R}^{n \times k}$ be the first k LB eigenfunctions of \mathcal{M}_1 , and $F \in \mathbb{R}^{n \times \ell}$ be ℓ feature functions. Similarly, we write $\mathbb{M}_2, \mathbb{S}_2$ as the mass and stiffness matrices of \mathcal{M}_2, Ψ as the first k LB eigenfunctions of \mathcal{M}_2 (under w^2g_2) that we would like approximate, and G as ℓ corresponding feature functions, ordered the same as in F. We also write w^2 as the discretized conformal factor on \mathcal{M}_2 and diag(w) as a diagonal matrix.

¹ In fact, we do not need to require that the surfaces have the same number of points, but doing so for now will allow for more convenient notation.

Therefore, the discretized optimization model (6) can be written as:

$$(w^*, \Psi^*) = \arg\min_{w, \Psi} \frac{r_1}{2} \| F^\top \mathbb{M}_2 \Phi - G^\top \operatorname{diag}(w) \mathbb{M}_2 \operatorname{diag}(w) \Psi \|_F^2 + \frac{r_2}{2} \operatorname{tr}(\Psi^\top \mathbb{S}_2 \Psi) + \frac{r_3}{2} w^\top \mathbb{S}_2 w,$$

$$\text{s.t.} \quad \Psi^\top \operatorname{diag}(w) \mathbb{M}_2 \operatorname{diag}(w) \Psi = \mathbf{I}_k, \quad \text{and} \quad w^\top \mathbb{M}_2 w = A$$

$$(9)$$

Here \mathbf{I}_k is the $k \times k$ identity matrix and $A = \sum_{i=1}^n \mathbb{M}_1(i,i)$. Since \mathbb{M}_2 is symmetric positive definite and diagonal, we can easily calculate the matrix decomposition $\mathbb{M}_2 = \mathbb{L}^\top \mathbb{L}$. If we also substitute $\bar{\Psi} = \mathbb{L} \operatorname{diag}(w)\Psi$, then (9) can be written as:

$$(w^*, \bar{\Psi}^*) = \arg\min_{w, \bar{\Psi}} \mathcal{E}(w, \bar{\Psi}) = \frac{r_1}{2} \|F^{\top} \mathbb{M}_1 \Phi - G^{\top} \operatorname{diag}(w) \mathbb{L}^{\top} \bar{\Psi}\|_F^2 + \frac{r_2}{2} \operatorname{tr}(\bar{\Psi}^{\top} \bar{\mathbb{S}}_2(w) \bar{\Psi}) + \frac{r_3}{2} w^{\top} \mathbb{S}_2 w,$$
s.t. $\bar{\Psi}^{\top} \bar{\Psi} = \mathbf{I}_k$ and $w^{\top} \mathbb{M}_2 w = A$ (10)

where $\bar{\mathbb{S}}_2(w) = (\mathbb{L}^\top)^{-1} \operatorname{diag}(w)^{-1} \mathbb{S}_2 \operatorname{diag}(w)^{-1} \mathbb{L}^{-1}$. Note that this parameterization of the problem moves the conformal factor w out of the orthogonality constraint (and into $\bar{\mathbb{S}}$). We will soon see that, for any fixed $\bar{\Psi}$, this will make the problem for w easier to solve.

4.2 Numerical Optimization of LBBP Model

The two variables w and $\bar{\Psi}$ in (10) make the optimization problem different from orthogonality constrained problems solved by nonconvex alternating direction method of multipliers (ADMM) methods considered in [23, 25, 52, 53]. Rather than solve this problem directly for $\bar{\Psi}$ and w simultaneously by directly minimizing (10), we employ a method based on the framework of proximal alternating minimization (PAM) method [1]. Let $S = \{\bar{\Psi} \in \mathbb{R}^{n \times k} \mid \bar{\Psi}^{\top}\bar{\Psi} = \mathbf{I}_k\}$ and $W = \{w \in \mathbb{R}^n \mid w^{\top}\mathbb{M}_2 w = A\}$. We also define indicator functions

$$\delta_{\mathcal{S}}(x) = \begin{cases} 0, & \text{if } x \in \mathcal{S} \\ +\infty, & \text{otherwise} \end{cases}, \qquad \delta_{\mathcal{W}}(x) = \begin{cases} 0, & \text{if } x \in \mathcal{W} \\ +\infty, & \text{otherwise} \end{cases}$$
(11)

Then it is clear that $\delta_{\mathcal{S}}$ and $\delta_{\mathcal{W}}$ are semi-algebraic functions as \mathcal{S} and \mathcal{W} are zero sets of polynomial functions [2]. Therefore, we write an equivalent form of (10) as

$$(w^*, \bar{\Psi}^*) = \arg\min_{w, \bar{\Psi}} \mathcal{E}(w, \bar{\Psi}) + \delta_{\mathcal{S}}(\bar{\Psi}) + \delta_{\mathcal{W}}(w). \tag{12}$$

Using the PAM method, we have the following iterative scheme

$$\begin{cases}
\bar{\Psi}^{j+1} = \arg\min_{\bar{\Psi}} \mathcal{E}(w^{j}, \bar{\Psi}) + \frac{1}{2\eta} ||\bar{\Psi} - \bar{\Psi}^{j}||^{2}, & \text{s.t. } \bar{\Psi}^{\top} \bar{\Psi} = \mathbf{I}_{k} \\
w^{j+1} = \arg\min_{w} \mathcal{E}(w, \bar{\Psi}^{j+1}) + \frac{1}{2\eta} ||w - w^{j}||^{2}, & \text{s.t. } w^{\top} \mathbb{M}_{2} w = A
\end{cases}$$
(13)

Here η is a step size parameter. These proximal terms penalizes large step sizes in and prevents the algorithm from "jumping" between multiple local minimums. The addition of these proximity terms allows us to analyze the proposed method in the framework of the PAM algorithm [1]. It has been shown in [1, 2, 8] that such proximal terms can guarantee the solutions generated at each step converge to a critical point of the objective function. Formally, we have the following convergence theorem in accordance with Theorem 9 in [1].

Theorem 1 Let $\{w^j, \bar{\Psi}^j\}$ be the sequence produced by (13), then the following statements hold:

1.
$$\mathcal{E}(w^{j+1}, \bar{\Psi}^{j+1}) + \frac{1}{2\eta} ||\bar{\Psi}^{j+1} - \bar{\Psi}^{j}||^2 + \frac{1}{2\eta} ||w^{j+1} - w^{j}||^2 \le \mathcal{E}(w^{j}, \bar{\Psi}^{j}), \ \forall j \ge 0.$$

2.
$$\sum_{j=1}^{\infty} (\|w^j - w^{j-1}\|^2 + \|\bar{\Psi}^j - \bar{\Psi}^{j-1}\|^2) < \infty.$$

3. $\{w^j, \bar{\Psi}^j\}$ converges to a critical point of $\mathcal{E}(w, \bar{\Psi})$.

Proof To prove this, we show that our model obeys the conditions required for local convergence of PAM in [1]. To do so, we need:

- (1) Terms which contain only one primal variable are bounded below and lower semicontinous.
- (2) Terms which contain both variables are C^1 and have a locally Lipschitz continuous gradients.
- (3) The entire objective satisfies the Kurdyka-Lojasiewicz (KL) property.

It is immediately clear that that the first two properties are satisfied by our objective. Furthermore, it is known that all semi-algebraic functions have KL property [1, 2, 53]. Our objective is semi-algebraic so we can guarantee local convergence of the proposed optimization method.

We use the augmented Lagrangian method to solve the constrained sub-optimization problem for w in (13). For convenience, let's write

$$\mathcal{L}(\bar{\Psi}, w; b) = \mathcal{E}(w, \bar{\Psi}) + \frac{r_4}{2} \left(w^{\top} \mathbb{M}_2 w - A + b \right)^2$$
(14)

Overall, we solve (10) in the following way by hybridizing PAM with the augmented Lagrangian method.

$$\begin{cases}
\bar{\Psi}^{j+1} = \arg\min_{\bar{\Psi}} \mathcal{E}(w^{j}, \bar{\Psi}) + \frac{1}{2\eta} ||\bar{\Psi} - \bar{\Psi}^{j}||^{2} \quad \text{s.t.} \quad \bar{\Psi}^{\top} \bar{\Psi} = \mathbf{I}_{k} \\
w^{j+1} \leftarrow \begin{cases}
w^{j+1,s+1} = \arg\min_{w} \mathcal{L}(w, \bar{\Psi}^{j+1}; b^{j+1,s}) + \frac{1}{2\eta} ||w - w^{j}||^{2} \\
b^{j+1,s+1} = b^{j+1,s} + (w^{j+1,s+1})^{\top} \mathbb{M}_{2} w^{j+1,s+1} - A.
\end{cases}$$
(15)

The subproblems for minimizing $\bar{\Psi}$ require a some special consideration. The main challenge this first sub-optimization problem is the nonconvex orthogonality constraints. Recently, several approaches have been developed to solve orthogonally constrained problems in feasible or infeasible ways [23, 25, 52, 53, 54]. For our implementation, we have chosen the feasible approach developed in [54] which uses a curvilinear method based on the Cayley transform together with Barzilai-Bowein step size line search. This method updates variables along a geodesic curve on the Stiefel manifold, a geometric description of the orthogonality. It preserves the orthogonality constraints and guarantees convergence to critical points in our scenario. More precisely, given a feasible starting point $\bar{\Psi}^s$ and the coordinate gradient Y^s at this point, the update scheme is as follows:

$$\begin{cases}
D^{s} = Y^{s}(\bar{\Psi}^{s})^{\top} - \bar{\Psi}^{s}(Y^{s})^{\top} \\
Q^{s} = (I + \frac{dt}{2}D^{s})^{-1}(I - \frac{dt}{2}D^{s}) \\
\bar{\Psi}^{s+1} = Q^{s}\bar{\Psi}^{s}
\end{cases} (16)$$

Here dt is a step size parameter chosen by the Barzilai-Bowein criteria developed in [4]. Although convergence to a global minimum is not guaranteed, this method has proven effective for our purposes and only requires the computation of the objective function and its coordinate gradient Y^s with respect to $\bar{\Psi}$ at each step provided by:

$$\nabla_{\bar{\Psi}} \left(\mathcal{E}(w, \bar{\Psi}) + \frac{1}{2\eta} ||\bar{\Psi} - \bar{\Psi}^j||^2 \right) = -r_1 G^{\top} \operatorname{diag}(w) \mathbb{L}^{\top} \left(F^{\top} \mathbb{M}_1 \Phi - G^{\top} \operatorname{diag}(w) \mathbb{L}^{\top} \bar{\Psi} \right)$$

$$+ r_2 \bar{\mathbb{S}}_2 \bar{\Psi} + \frac{1}{\eta} (\bar{\Psi} - \bar{\Psi}^j)$$

$$(17)$$

The subproblem for w (as written in (15)), on the other hand is smooth and unconstrained. For our implementation, we use the well known quasi-Newton BFGS algorithm [5]. The gradient of objective function with respect to w can be written as:

$$\nabla_{w} \left(\mathcal{L}(w, \bar{\Psi}; b) + \frac{1}{2\eta} ||w - w^{j}||^{2} \right) = r_{1} \operatorname{diag} \left(G^{\top}(F^{\top} \mathbb{M}_{1} \Phi - Gw \mathbb{L}^{\top} \bar{\Psi})) \bar{\Psi}^{\top} \mathbb{L} \right)$$

$$+ r_{2} \operatorname{diag} \left(\Psi \Psi^{\top} \mathbb{S}w^{-1} \right) \odot w^{-2}$$

$$+ r_{3} \mathbb{S}_{2}w + r_{4} \left(w^{\top} \mathbb{M}_{2}w - A + b \right) \mathbb{M}_{2}w + \frac{1}{n} (w - w^{j})$$

$$(18)$$

where $diag(\cdot)$ denotes the diagonal of the matrix, \odot signifies element-wise Hadamard product and w^{-2} is the inverse of diagonal matrix w multiplied with itself.

4.3 Computation of Point-to-Point Map

One naive way to compute a point-to-point map is to find the functional map by using the final deformed manifold and its LB eigensystem with respect to the deforantion. However, this may not work well because of the ambiguity of LB eigensystem. Additional effort is needed to handle possible ambiguity of LB eigensystem such as the method discussed in [26]. As an advantage of the proposed method, the resulting basis generated by the proposed algorithm (recovered as $\Psi^* = A^{-1}w\bar{\Psi}$) to will naturally correct ambiguities of LB eigensystem. This is similar to the method discussed in [22]. Thus, we can compute the functional map as $F_T(h) = \sum_{i=1}^k (\int_{\mathcal{M}_1} h\phi_i \ d\mathcal{M}_1)\psi_i^\top = \Psi\Phi^\top \mathbb{M}_1 h$. However, this method is still quite inefficient and may be sensitive to small errors in the resulting basis.

Instead, after we recover the final basis from our method, we can compute the point-to-point map between the two surfaces by comparing the values of each of the basis functions. This is essentially the same scheme presented in [32], but applied to our new basis. We use a KNN search (with K=1) to match rows of Φ and Ψ . This requires a search of n points in k dimension, but is much more efficient and accurate than using the delta function approach described in the previous paragraph. Other methods used to refine functional maps such as [37] can be applied in this setting without changes. We summarize our numerical method for nonisometric surface registration as Algorithm 1.

Algorithm 1: LB Basis Pursuit (LBBP) Algorithm.

Input: Triangulated surfaces \mathcal{M}_1 and \mathcal{M}_2 and list of known corresponding functions F and G. Output: Ψ^* , w, point-to-point map

- 1 Compute stiffness and mass matrices for each surface: M_1, M_2, S_1, S_2 ;
- **2** Use stiffness and mass to calculate LBO eigensystems: $\mathbb{M}_1 \Phi = \lambda \mathbb{S}_1 \Phi$;
- **3** Initialize: Let Ψ^0 be the LB eigenfunctions of target surface: $\mathbb{M}_2\Psi = \lambda \mathbb{S}_2\Psi$;
- 4 Compute $\bar{\Psi}^0 = \mathbb{L}w\Psi$;
- 5 while not converged do

```
 \begin{array}{ll} \mathbf{6} & \text{Update } \bar{\Psi}^{j+1} = \arg\min_{\bar{\Psi}} \mathcal{E}(w^{j}, \bar{\Psi}) + \frac{1}{2\eta} ||\bar{\Psi} - \bar{\Psi}^{j}||^{2} \text{ using the curvilinear search algorithm (16);} \\ \mathbf{7} & \textbf{while } s \leq \ell \text{ do} \\ \mathbf{8} & \text{Update } w^{j+1,s} = \arg\min_{w} \mathcal{L}(w, \bar{\Psi}^{j+1}; b^{j+1,s}) + \frac{1}{2\eta} ||w - w^{j}||^{2} \text{ using BFGS;} \\ \mathbf{9} & b^{j+1,s+1} = b^{j+1,s} + (w^{j+1})^{\top} \mathbb{M}_{2} w^{j+1} - A; \\ \mathbf{10} & w^{j+1} = w^{j+1,s}; \end{array}
```

- 11 Recover $\Psi^* = w \mathbb{L}^{-1} \bar{\Psi}$:
- 12 Compute correspondence map with KNN-search of coefficient space

5 Discussion

In this section, we discus our choice of feature functions, as well as ways to overcome problems which may arise from the non-convexity of the proposed optimization problem.

5.1 Choice of Feature Functions

The simplest, and in many applications, most natural features to choose for F and G are indicator functions for known landmarks. Let $\{x_i^1\}_{i=1}^k$ be a set of points on \mathcal{M}_1 and $\{x_i^2\}_{i=1}^k$ be a corresponding set on \mathcal{M}_2 . We can view each f_i and g_i as a δ -function on \mathcal{M}_1 and \mathcal{M}_2 respectively to indicate these landmarks.

Another option is to use heat diffusion functions. Given a corresponding pair of points we can use delta functions to define an initial condition and solve the heat diffusion problem $\frac{\partial u}{\partial t}(x) = \Delta u(x,t)$ using the

Crank-Nicholson scheme $\left(\mathbb{M} + \frac{dt}{2}\mathbb{S}\right)u^{i+1} = \left(\mathbb{M} - \frac{dt}{2}\mathbb{S}\right)u^i$ where dt is a step size parameter. By taking "snap shots" (solutions of the equation for various t values) of u at different time values, we can generate multiple functions from a single corresponding pair. This choice allows for a multi-scale selection of features and often results in better correspondences, although it is computationally more expensive. Also, since the heat diffusion is sensitive to local geometry, it is often necessary to recompute the diffusion with respect to the conformal factor. This can be included as a step in the reinitialization scheme which will be discussed in the next section.

The wave kernel signature (WKS) has also been used for characterizing points on non-rigid three dimensional shapes [3]. These functions are defined as the solutions to the Schrodinger equation: $\frac{\partial u}{\partial t}(x) = i\Delta u(x,t)$ at different points on the surface. Given two corresponding points we can solve the equation at each point and use these as our corresponding functions. However, the solutions to these equations are highly dependent on both local and global geometries of the manifold. Because of this, they are only suitable for shape correspondence when the shapes are very similar and, in general, do not work well for non-nearly-isometric problems. The same problem exists for heat diffusion features, however, in general heat diffusion tends to be much more stable with respect to local deformations.

SHOT features [48] are also a popular choice of feature functions for shape processing tasks. For nearly isometric shapes these descriptors work well, but since they are not intrinsically defined they do not work well with the re-initialization scheme detailed in the next section. Updating these features with respect to a conformal deformation requires computing the deformed embedding, which the rest of our method explicitly avoids.

5.2 Reinitialization Schemes

Although we have shown that the proposed PAM based optimization algorithm converges to a critical point of the objective function, it is still challenging to achieve a global optimum as the problem is non-convex. In practice, we have found that the numerical results can often be improved in terms of both accuracy and speed of computation by adding a simple reinitialization scheme to our algorithm. The motivation for the scheme comes from an observation that if we know the exact conformal deformation w^2 and the source surface has a simple eigensystem (no repeated eigenvalues), then the LB eigensystem of (\mathcal{M}_1, g_1) is the same as the LB eigensystem of (\mathcal{M}_2, w^2g_2) up to a change in sign. With this in mind, we propose to reinitialize the Ψ problem by resetting Ψ to be the solution to weighed eigenproblem $\mathbb{S}_2\Psi = \Lambda \mathrm{diag}(w^2)\mathbb{M}_2\Psi$. We remark that this reinitialization method to achieve an optimizer closer to the global one is empirical, although it is based on the geometric intuition.

Computationally, to avoid introducing ambiguities of LB eigensystem by calling a standard eigen-solvers, we solve a discrete counterpart to (4) as $\min_{\Psi} \operatorname{tr}(\bar{\Psi}^{\top}\bar{\mathbb{S}}_{2}(w)\bar{\Psi})$, s.t. $\bar{\Psi}^{\top}\bar{\Psi}=\mathbf{I}$ based on the curvilinear search method discussed in Section 4.2 and using the current eigensystem, $\bar{\Psi}^{j+1}$, as an initial guess for this problem. By using $\bar{\Psi}^{j+1}$ as warm start for the eigenproblem we can avoid re-introducing sign or multiplicity ambiguities into the problem which our algorithm has already resolved.

When using heat diffusion, wavelet kernel signatures, or any other functions which are defined based on local geometry as the input feature functions, then we also need to recalculate these functions with respect to the conformally deformed metric. For example, if we are using heat diffusions, we can recompute the heat diffusion functions on the deformed manifold $(\mathcal{M}_2, w^2 g_2)$ by multiplying the mass matrix by w^2 in the Crank-Nicholson scheme: $\left(\mathbb{M}_2 \mathrm{diag}(w^2) + \frac{dt}{2}\mathbb{S}_2\right)u^{i+1} = \left(\mathbb{M}_2 \mathrm{diag}(w^2) - \frac{dt}{2}\mathbb{S}_2\right)u^i$, A similar re-computation technique can be applied to wave kernel signatures, or any other features which are computed using finite element-like operators.

5.3 Sub-sampling scheme

The most computationally demanding step of our algorithm is the update of $\bar{\Psi}$. As a result, the time complexity of our algorithm depends on the number of points in the discretization of \mathcal{M}_2 . However, the

overall geometry of the shape can often be closely estimated by a relatively small subset of the points contained in a triangulated mesh or point cloud. Inspired by this observation, we propose a warm start method in which we solve a smaller problem on a subset of the full mesh and use it as a warm start for the full problem. One way to do this would be to sub-sample the mesh and compute a new (local) triangulation [29]. However, the re-meshing process can be computationally expensive. Therefore, we instead seek a method to approximate $\bar{\Psi}$ on the entire mesh, using only the sub-sampled points.

Given a mesh M with n points, we first compute a sub-sample of points \bar{M} with $\bar{n} < n$ points which most articulately represents the original mesh. To do so, we begin with a random seed point and compute the point on the mesh which has the greatest (geodesic) distance from it and include this point in \bar{M} . Then we iteratively add points to \bar{M} by finding the point on M which has the greatest minimal distance to any point already included in \bar{M} .

Algorithm 2: Subsampling and Warm Start Algorithm.

Input: Set of vertices and faces of source (\mathcal{M}_1) and target (\mathcal{M}_2) manifolds, number of subsample points \bar{n} , list of known corresponding functions F and G, Stiffness and Mass Matrices $\mathbb{S}_1, \mathbb{S}_2, \mathbb{M}_1, \mathbb{M}_2$

Output: Ψ^* , w^* ,

- 1 Initialize: Let Ψ be the LBO eigenfunctions of target surface: $\mathbb{M}_2\Psi = \lambda \mathbb{S}_2\Psi$;
- **2** Compute downsampled points to represents \mathcal{M}_1 ;
- **3** Compute down sampled bases and representation of F;
- 4 Use Algorithm 1 to solve (20) for D^*, C^* ;
- 5 Compute $\bar{\Psi} = \sum_{i=1}^{\bar{n}} C_i u_i$ and $w = \sum_{i=1}^{\bar{n}} D_i u_i$;

To approximate a function f defined on M with only \bar{n} variables, we define linear projection and reconstruction operations to down-sample the problem. One naive idea would be to restrict the values of f to \bar{M} and use linear interpolation in the other direction. However, this fails to capture many of the details of functions in the projection step, and doesn't respect the local geometry in the reconstruction step. Instead, we use a new approximate basis with elements, $U = \{u_i : M \to \mathbb{R}\}_{i=1}^{\bar{n}}$, created by diffusing a delta function on M, centered at each point on \bar{M} for a fixed time t. The resulting basis contains \bar{n} elements. We define a projection operation and reconstruction operations as

$$Proj(f) := (U^{\top} \mathbb{M} U)^{-1} U^{\top} \mathbb{M} f = \bar{f}$$

$$Recon(\bar{f}) := \bar{f} U$$
(19)

We can then use this new approximate basis to reduce the dimension of the optimization problem and solve the simplified problem very quickly. We consider the projection of Ψ and w onto the $\{u_i\}$ set which can be represented as the coefficients $C_i = \langle \bar{\Psi}, u_i \rangle$ and $D = \{\langle w, u_i \rangle\}_i$. Plugging these into our model we get:

$$(D^*, C^*) = \arg\min_{D,C} \mathcal{E}(D, C) = \frac{r_1}{2} \| F^{\top} \mathbb{M}_1 \Phi - G^{\top} \operatorname{diag}(DU) \mathbb{L}_U^{\top} C \|_F^2 + \frac{r_2}{2} \operatorname{tr}(C^{\top} \bar{\mathbb{S}}_{U2} C) + \frac{r_3}{2} D^{\top} \mathbb{S}_{U2} D,$$
s.t. $C^{\top} U^{\top} U C = \mathbf{I}_n$ and $w^{\top} \mathbb{M}_{u2} w = A$ (20)

Where $\mathbb{M}_{U2} = U^{\top} \mathbb{M}_1 U$, $\mathbb{L}_U = U^{\top} \mathbb{L}$, $\bar{\mathbb{S}}_{U2} = U^{\top} \bar{\mathbb{S}}_2 U$ and $\mathbb{S}_{U2} = U^{\top} \mathbb{S}_2 U$ can all be precomputed. Note that if $\{u_i\}_{i=1}^{\bar{n}}$ is, in fact, a tight frame then (20) is the same as (8). This problem can be solved with algorithm (1), but has significantly fewer variables then (8). By using using the elongation of the solution to (20) as an initial guess for $\bar{\Psi}$ and w we can significantly decrease the time needed to solve the full model.

With this warm start algorithm 2 and the re-initialization procedure described in Section 5.2, we propose a modified version of our numerical solver as Algorithm 3.

6 Numerical Experiments

In this section, we apply our algorithm to several problems. We begin by working on a typical non-isomorphic matching problem for a pair of shapes with a large deformation: a horse and an elephant. We preform tests

Algorithm 3: LB Basis Pursuit Algorithm with warm start and reinitialization.

```
Input: Set of vertices and faces of source (\mathcal{M}_1) and target (\mathcal{M}_2) manifolds and list of known
                corresponding functions F and G
    Output: \Psi^*, w^*, point-to-point correspondence map
 1 Compute stiffness and mass matrices for each surface: M_1, M_2, S_1, S_2;
 2 Use stiffness and mass to calculate LBO eigensystems: \mathbb{M}_1 \Phi = \lambda \mathbb{S}_1 \Phi;
 3 Compute corresponding feature functions F and G on \mathcal{M}^1 and \mathcal{M}^2 respectively;
 4 Initialize: Let \Psi^0 be the LBO eigenfunctions of target surface: \mathbb{M}_2\Psi = \lambda \mathbb{S}_2\Psi;
    Compute down sampled bases through downsample and heat diffusion;
    Compute \bar{\Psi}^0 and \bar{w}^0 through warm start through Algorithm 2;
     while number of re-initialization steps complete < max number of re-initializations do
         Update \bar{\Psi}^{j+1} = \arg\min_{\bar{\Psi}} \mathcal{E}(w^j, \bar{\Psi}) + \frac{1}{2\eta} ||\bar{\Psi} - \bar{\Psi}^j||^2 using the curvilinear search algorithm (16);
 8
         while s \le \ell do
 9
               \begin{aligned} \text{Update } w^{j+1,s} &= \arg\min_{w} \mathcal{L}(w, \bar{\Psi}^{j+1}; b^{j+1,s}) + \frac{1}{2\eta} ||w-w^{j}||^{2} \text{ using BFGS}; \\ b^{j+1,s+1} &= b^{j+1,s} + (w^{j+1})^{\top} \mathbb{M}_{2} w^{j+1} - A; \end{aligned} 
10
11
          w^{j+1} = w^{j+1,l}:
12
          \mathbf{if} \ \mathit{update} < \mathit{tolerance} \ \mathbf{then}
13
              Re-Initialize \bar{\Psi} as \arg\min_{\bar{\Psi}} \ \mathrm{tr}(\bar{\Psi}^{\top}\bar{\mathbb{S}}_{2}(w^{j+1})\bar{\Psi}), \ \mathrm{s.t.} \ \bar{\Psi}^{\top}\mathbb{M}_{2}\bar{\Psi} = \mathbf{I};
14
               if Using feature functions which depend on local geometry then
15
                    Re-Compute features using M_2 \operatorname{diag}(w^2) as Mass matrix
16
17 Compute correspondence map with KNN-search of coefficient space
```

showing the effectiveness of our approach given different amounts of landmark points, and demonstrate robustness with respect to noise both on the manifold and in the initial correspondences. We further conduct experiments on the Faust benchmark data set [7] and conduct comparisons with several existing methods. All numerical experiments are implemented in MATLAB on a PC with a 32GB RAM and two 2.6GHz CPUs.

In all of our experiments, we use randomly chosen correspondence points to create indicator functions as the input features. The first 100 non-trivial LB eigenfunctions are chosen to calculate the coefficient matching term, as well as for computing the final correspondence. We set $r_1 = 10$, $r_2 = 10$, $r_3 = 1$, $r_4 = .01$, $\ell = 1$ for all experiments, even though the data sets and experimental conditions are very different. This choice of r_1 and r_2 allows the coefficient matching terms and eigenfunction term to balance each other out, with the choice of r_3 still being large enough to preserve the area constraint. r_4 is chosen to be small so that the harmonic energy, which tends to be quite large, does not dominate the others. In general, we have observed that our algorithm is quite robust to different choices of parameters.

6.1 A Large Deformation Pair: Horse to Elephant

The first experiment is designed to test the effectiveness of the proposed method on a pair of shapes with large deformation. Each surface, a horse and an elephant, is represented by a mesh with 1200 points. One of the challenges in this pair is the large deformations in the sharp corner and elongated regions such as ears, teeth, noses and tails on the horse and elephant surfaces. Those regions make the registration problem very challenging. To demonstrate the efficacy of our approach, we perform this experiment under several different conditions. Our algorithm produces excellent results given a sufficient number of landmarks, and it still finds reliable correspondences given limited landmarks. We also show that using our reinitialization scheme (Algorithm 3) produces a more accurate map than without this extra step (Algorithm 1).

Qualitative illustration The left panel of Figure 1 shows the convergence of the objective function and illustrates the effectiveness of the reinitialization step. We plot the three terms in the objective function

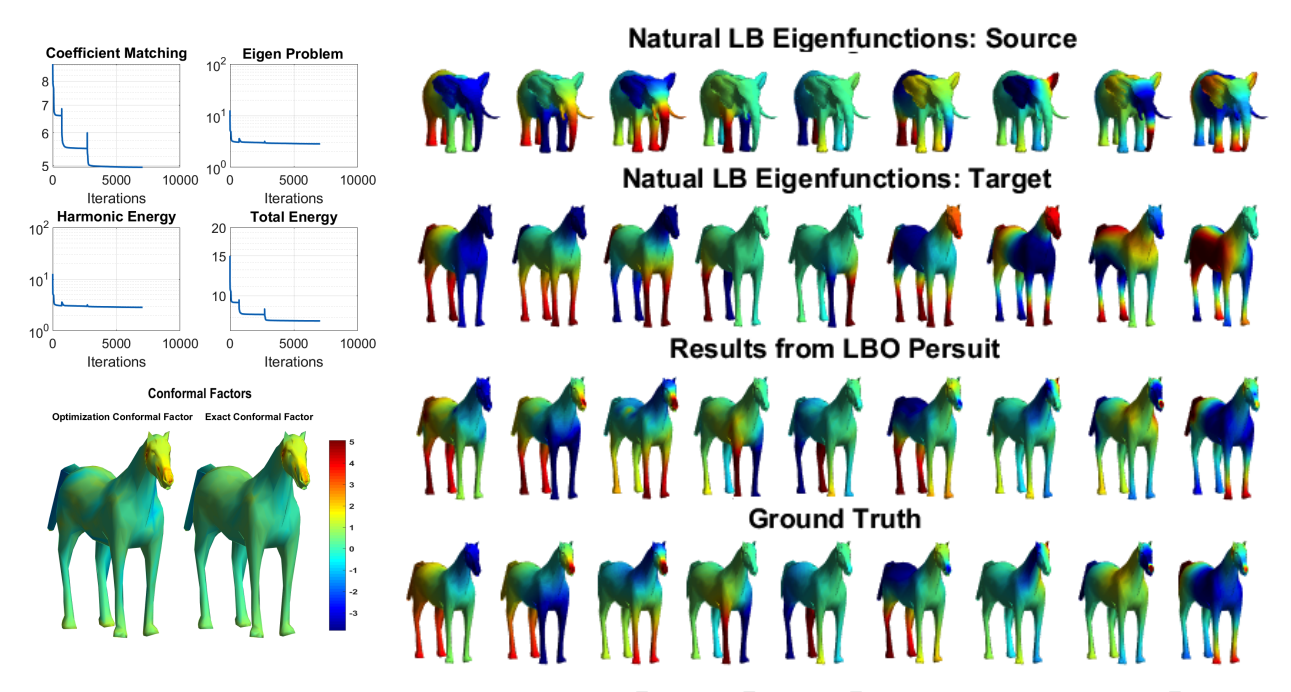


Fig. 1 Left top: The coefficient matching term measures: $||F^{\top}\mathbb{M}_{1}\Phi - G^{\top}\operatorname{diag}(w)\mathbb{L}^{\top}\bar{\Psi}||_{F}$. The eigen problem is: $(\Psi^{\top}\mathbb{S}_{2}\Psi)$ and the harmonic energy measures: $w^{\top}\mathbb{S}_{2}w$ and the total energy is the entire model derived in (10). Left bottom: resulting and exact conformal factors. Right panel: First two rows: The first 9 non-trivial natural LB eigenfunctions of manifolds. The third row: results from the proposed basis pursuit algorithm. The fourth row: ground truth. Left: convergence curves of our method.

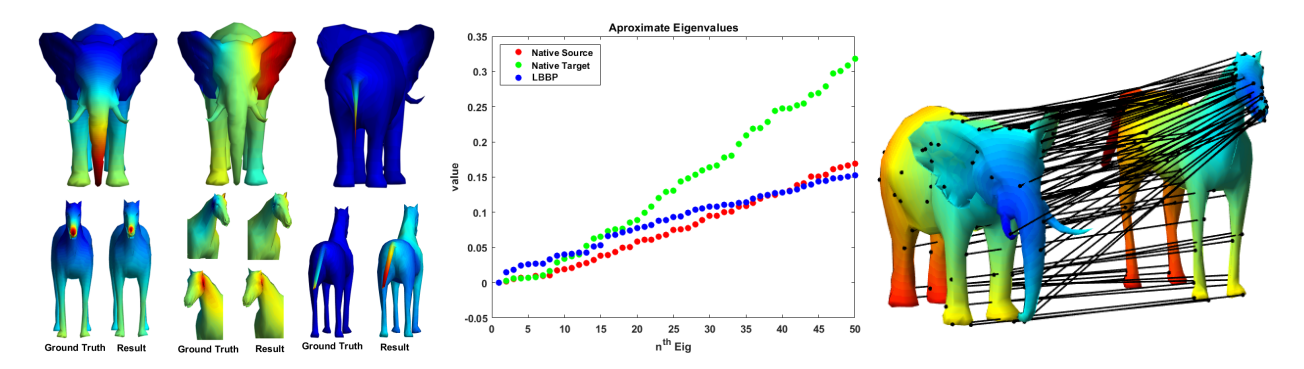


Fig. 2 Top left: 9th, 11th and 44th natural LB eigenfunctions on source. Bottom left: results and ground truth. Middle: Alignment of the LB eigenvalues. Right: visualization of point-to-point map and texture transfer.

separately as well as the overall objective. We typically observe that the convergence curves in the coefficient matching and total energy flatten quickly as the algorithm tends to a local minimizer. More importantly, each reinitialization significantly reduces the objective function. We further demonstrate the validity of our algorithm by examining the resulting conformal factor. In the left bottom image of Figure 1, we show the conformal factor calculated by our algorithm as well as the ground truth. The ground truth conformal factor is calculated by using the ground truth point-to-point map to compare the area of the first ring structure around each point on the source and target surface respectively. Here we plot u where $u^2 = e^{2u}$ for better visualization. From this figure we can confirm that the produced conformal factor from our algorithm is very close to the true factor.

Since the elephant and horse are dramatically different shapes, the large dissimilarity of their natural LB eigenfunctions (first two rows of the right panel in Figure 1) cannot be expected to produce meaningful correspondence. However, our model overcomes this by capturing the conformal deformation between the surfaces. As results plotted in the third of the right panel in Figure 1, the basis computed for the horse (target surface) by our model is consistent with the LB eigenfunctions of the elephant (source surface). We

further compare these results with the ground truth (showed in fourth row of the right panel in Figure 1) which is calculated through the push forward of the LB eigenfunction of the source to the target surface using the ground truth map. This comparison also confirms that functions obtained from the proposed model produces satisfactory results. Moreover, We highlight the consistency of the produced bases on several highly distorted regions including ears, nose/trunk and the tails in the left picture of Figure 2. All of these results visually illustrate that our approach produces a new basis on the target that aligns very closely to the natural LB basis on the sources manifold. As an additional evidence, the middle picture in Figure 2 shows that the eigenvalues of the deformed eigenesytem are much closer to the eigenvalues of the source surface than they are to the target. Although these values are never explicitly taken into account in our numerical algorithm, it is not surprising that aligning the eigenfunctions also aligns their eigenvalues. This close alignment of the eigensystems is the reason that accurate registration results can be obtained using the new basis. Finally, we visually show the obtained high quality point-to-point correspondence based on the resulting basis.

Quantitative illustration Next, we quantitatively demonstrate the dependence of the performance on the number of given landmarks, the effectiveness of the sub-sampling scheme, the necessity of using conformal deformation as well as the robustness of our method to noisy data and landmark perturbation. To quantitatively measure the mapping quality, we calculate the normalized geodesic distance from the point on the target surface produced by the map to ground truth following the Princeton Benchmark method [21]. These distances are collected into a cumulative error plot where the y-axis measures the percent of points whose distances are less than or equal to the x-axis value.

The left picture in Figure 3 shows geodesic errors of correspondence using 100, 75, 50 and 25 known landmark points with and without our reinitialization scheme. It is reasonable to see that the algorithm with more landmarks provide better numerical performance. For example, in the case of 100 known landmarks, our algorithm matches over 70% of the points to exact correct point and more than 98% within a 5% error margin. This is certain more accurate than the correspondence obtained from 25 landmark points although it still provides a very good corresponding result.

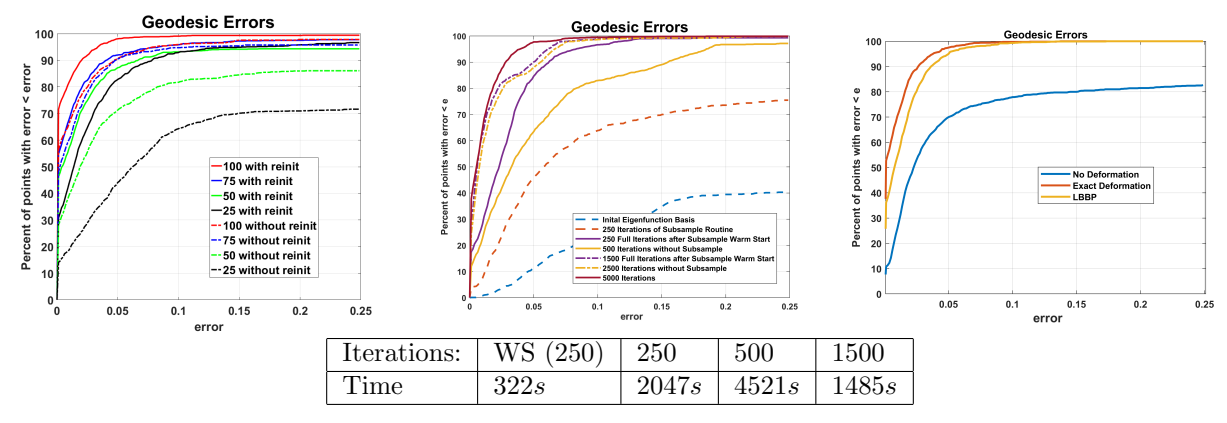


Fig. 3 Left:normalized geodesic errors for various numbers of randomly selected landmarks with and without reinitialization. Middle: Quality of correspondences produced at various stages of our algorithm, with and without warm start (WS). Right: Comparisons of results obtained from basis pursuit without deformation, with oracle deformation and our LBBP method.

To illustrate the effectiveness of the sub-sampling scheme presented in section 5.3, we repeat the previous experiment twice more, both with and without the sub-sampling warm start, and manually stop the algorithm after 500 iterations. The middle picture in Figure 3 shows the quality of the correspondences produced by the initial basis, the one produced by the sub-sampling scheme after 250 iterations, the basis produced by algorithms after 250 full iterations using the sub-sampled scheme as a warm start, one produced by the algorithm using 500 iterations of the full scheme without using the warm start and finally results after 1500 and 2500 iterations with and without the warm start. From this figure we observe that the warm start routine can significantly speed up the basis pursuit by providing a good initialization to the full algorithm.

To show the importance of understanding the deformation between surfaces when using a spectral based method, we run two tests for finding correspondence between horse and elephant using LB basis pursuit

algorithm but freezing the conformal deformation. We first set the conformal factor to be 1 everywhere. This mean no deformation is imposed in the procedure of the LB basis pursuit. Next, we use the exact deformation, which can be computed as a priori using the exact correspondence. The right image in Figure 3 shows the geodesic errors of the correspondence produced by the optimized bases when using each of these fixed conformal factors, as well as the result of our algorithm referred as LBBP. Although, our algorithm does not achieve the same performance as using the oracle deformation (which is not obtainable in practice), we vastly outperform the non-deformation case.

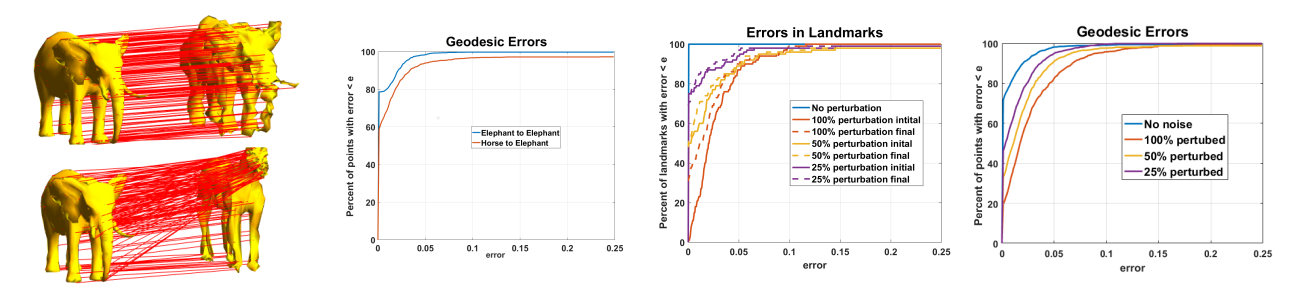


Fig. 4 Left to right: point-to-point maps for noisy data, normalized geodesic errors for noisy data, Initial perturbations to landmarks and final error of landmarks, and final registration geodesic errors for all points using perturbed landmarks.

Next, we demonstrate that our algorithm enjoys robustness and flexibility of handling noisy data. Since noise on the surfaces can be viewed as local deformations, our algorithm is automatically robust to geometric noise. Medical scans often have noise resulting from the imaging instruments and manual segmentation. Our model can solve registration problems for this type of data. To demonstrate this, we generate noisy data by adding noise along the normal of each point. The left two pictures in Figure 4 shows the results of two experiments: a noisy elephant to an elephant and a noisy horse to an elephant. We observe that our algorithm still produces very accurate results despite this noise.

We also demonstrate the robustness of our algorithm to landmark perturbations. Working again on the horse and elephant, we test cases where the landmarks are perturbed to another vertex within the first ring. The magnitude of these perturbations depends on the uniformity and meshing of the surface. The second most right picture in Figure 4 shows the size of the perturbations of the landmarks points as well as the error in their final mapping. The most right picture in Figure 4 compares the geodesic error of the for all points when 25%, 50% and 100% of the landmarks points are perturbed. From these tests we conclude that our method can successfully reduce the error introduced in the perturbed landmarks and still produce accurate maps in the presence of perturbations.

6.2 Benchmark test using the Faust Data set

In our next experiment, we test our algorithm on a larger data set to demonstrate its effectiveness and robustness on a variety of shapes. The Faust dataset is a collection of $100\ 3D$

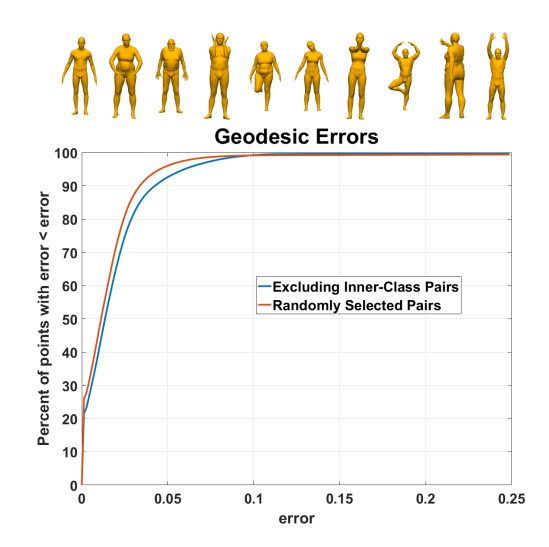


Fig. 5 Geodesic errors for randomly selected and least isomorphic pairs.

shapes composed of 10 real individuals in 10 distinct poses. Instead of testing all 9900 possible correspondences be each of the pairs, we select two smaller subsets of shapes to formulate to smaller test sets. For the first test, we randomly choose 100 pairs of shapes and compute the correspondences. In the second test, we choose 10 scans and ensure that each individual and each pose is represented exactly once in the test set and compute all 90 correspondence maps. (Figure 5) [7]. This selection criteria ensures that no pairs are from

the same the pose or individual. The bottom left graph in Figure 5 shows the average error of the mappings for each of these tests. We see that our algorithm again computes very accurate correspondences for both tests. Furthermore, we see that the results for the harder test set are very close to the results for the first test set. This indicates that our approach can effectively handle non-isometric matching problems with large deformations. For each of these test we employ our sub-sampling scheme outlined in Algorithm 2, using a subsample of 1000 points to compute a basis which we use as a warm start for the dense meshes. Each pair took roughly 45 minutes to compute.

6.3 Comparisons with Other Nonisometric Techniques

Figure 6 shows the a comparison our algorithm and that of the kernel matching [51], coupled quasi-harmonic basis [22], basis matching (no deformation in 6.2) and functional maps [32] approaches on the non-isometric horse to elephant problem and on a nearly isometric problem taken from the FAUST dataset. For each test the algorithms used 100 randomly generate heat diffusion functions as corresponding features and solve the minimization problem until the relative objective function update falls below 10e-6.

The horse-to-elephant test has a much larger deformation, but is also much less densely meshed. As a result the algorithms which are able to encapsulate the change in local geometry, kernel matching and our approach perform much better than methods developed for near-isometric surfaces. On the other hand the problem taken from the Faust data set has a much smaller deformation, so methods which rely on the native eigensystems being closely aligned (functional maps and coupled basis) perform much better on this test then on the horse-to-elephant case. All of these comparisons show that our method produces more accurate mapping than those from the state-of-the-art methods.

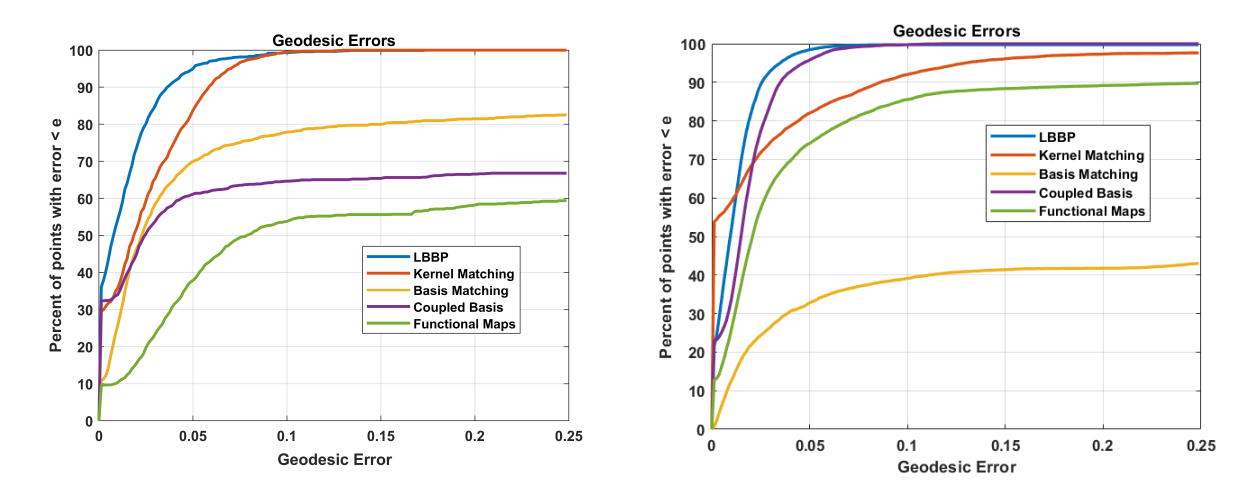


Fig. 6 Left: Comparison of methods on non-isometric horse-to-elephant. Right: Comparison of methods on FAUST data set.

7 Conclusions

In this work, we have developed a variation method for computing correspondence between pairs of largely deformed non-isometric manifolds. Our approach considers conformal deformation of the manifolds and combines with traditional LB spectral theory. This method naturally connects metric deformations to the spectrum of the manifold and therefore allows us to register manifolds with large deformations. Our approach simultaneously aligns the bases of the manifolds and computes a conformal deformation without having to explicitly reconstruct the deformed manifolds. We have also proposed an efficient, locally convergent method to solve this model based on the PAM framework. Finally, we have conducted intensive numerical experiments to demonstrate the effectiveness and robustness of our methods.

Declarations

Funding The research of S. Schonsheck and R. Lai is supported in part by NSF DMS-1522645 and an NSF Career Award DMS-1752934. M. Bronstein is partially supported by ERC Consolidator grant No. 724228 (LEMAN).

Conflicts of interest/Competing interests The authors declare no conflicts of interest/competing interests.

Availability of data and material The datasets generated during and/or analysed during the current study are available in the FAUST repository (http://faust.is.tue.mpg.de).

Code availability Source codes are available upon request.

Authors' contributions R. Lai and M. Bronstein designed the research. R. Lai and S. Schonsheck performed the research and wrote the paper.

References

- 1. Attouch H, Bolte J, Redont P, Soubeyran A (2010) Proximal alternating minimization and projection methods for nonconvex problems: An approach based on the kurdyka-łojasiewicz inequality. Mathematics of Operations Research 35(2):438–457
- 2. Attouch H, Bolte J, Svaiter BF (2013) Convergence of descent methods for semi-algebraic and tame problems: proximal algorithms, forward–backward splitting, and regularized gauss–seidel methods. Mathematical Programming 137(1-2):91–129
- 3. Aubry M, Schlickewei U, Cremers D (2011) The wave kernel signature: A quantum mechanical approach to shape analysis. In: Computer Vision Workshops (ICCV Workshops), 2011 IEEE International Conference on, IEEE, pp 1626–1633
- 4. Barzilai J, Borwein JM (1988) Two-point step size gradient methods. IMA journal of numerical analysis 8(1):141-148
- 5. Bazaraa MS, Sherali HD, Shetty CM (2013) Nonlinear programming: theory and algorithms. John Wiley & Sons
- 6. Bérard P, Besson G, Gallot S (1994) Embedding riemannian manifolds by their heat kernel. Geometric and Functional Analysis 4(4):373–398
- 7. Bogo F, Romero J, Loper M, Black MJ (2014) Faust: Dataset and evaluation for 3d mesh registration. In: Proceedings of the IEEE Conference on Computer Vision and Pattern Recognition, pp 3794–3801
- 8. Bolte J, Sabach S, Teboulle M (2014) Proximal alternating linearized minimization for nonconvex and nonsmooth problems. Mathematical Programming 146(1-2):459–494
- 9. Bronstein AM, Bronstein MM, Kimmel R (2006) Efficient computation of isometry-invariant distances between surfaces. SIAM Journal on Scientific Computing 28(5):1812–1836
- 10. Bronstein MM, Kokkinos I (2010) Scale-invariant heat kernel signatures for non-rigid shape recognition. IEEE Conference on Computer Vision and Pattern Recognition (CVPR) pp 1704–1711
- 11. Chavel I (1984) Eigenvalues in Riemannian geometry, vol 115. Academic press
- 12. Dziuk G, Elliott CM (2013) Finite element methods for surface pdes. Acta Numerica 22:289–396
- 13. Elad A, Kimmel R (2003) On bending invariant signatures for surfaces. IEEE Transactions on pattern analysis and machine intelligence 25(10):1285–1295
- 14. Glowinski R, Le Tallec P (1989) Augmented Lagrangian and operator-splitting methods in nonlinear mechanics. SIAM
- 15. Gu X, Wang Y, Chan TF, Thompson PM, Yau ST (2004) Genus zero surface conformal mapping and its application to brain surface mapping. IEEE Transactions on Medical Imaging 23(8):949–958
- 16. Haker S, Angenent S, Tannenbaum A, Kikinis R, Sapiro G, Halle M (2000) Conformal surface parameterization for texture mapping. IEEE Trans Visualization and Computer Graphics 6(2):181—189

- 17. Heimann T, Meinzer HP (2009) Statistical shape models for 3d medical image segmentation: a review. Medical image analysis 13(4):543–563
- 18. Hurdal MK, Stephenson K, Bowers P, Sumners D, Rottenberg D (2000) Coordinate systems for conformal cerebellar flat maps. NeuroImage S467
- 19. Jost J (2008) Riemannian geometry and geometric analysis. Springer Science & Business Media
- 20. Kao CY, Lai R, Osting B (2017) Maximization of laplace- beltrami eigenvalues on closed riemannian surfaces. ESAIM: Control, Optimisation and Calculus of Variations 23(2):685–720
- 21. Kim VG, Lipman Y, Funkhouser T (2011) Blended intrinsic maps. In: ACM Transactions on Graphics (TOG), ACM, vol 30, p 79
- 22. Kovnatsky A, Bronstein MM, Bronstein AM, Glashoff K, Kimmel R (2013) Coupled quasi-harmonic bases. In: Computer Graphics Forum, Wiley Online Library, vol 32, pp 439–448
- 23. Kovnatsky A, Glashoff K, Bronstein MM (2016) Madmm: a generic algorithm for non-smooth optimization on manifolds. In: European Conference on Computer Vision, Springer, pp 680–696
- 24. Kraevoy V, Sheffer A (2004) Cross-parameterization and compatible remeshing of 3d models. ACM Transactions on Graphics (TOG) 23(3):861–869
- 25. Lai R, Osher S (2014) A splitting method for orthogonality constrained problems. Journal of Scientific Computing 58(2):431–449
- 26. Lai R, Zhao H (2017) Multiscale nonrigid point cloud registration using robust sliced-wasserstein distance via laplace-beltrami eigenmap. SIAM Journal on Imaging Sciences 10(2):449–483
- 27. Lai R, Shi Y, Scheibel K, Fears S, Woods R, Toga AW, Chan TF (2010) Metric-induced optimal embedding for intrinsic 3D shape analysis. Computer Vision and Pattern Recognition (CVPR) pp 2871–2878
- 28. Lai R, Shi Y, Sicotte N, Toga AW (2011) Automated corpus callosum extraction via laplace-beltrami nodal parcellation and intrinsic geodesic curvature flows on surfaces. In: Computer Vision (ICCV), 2011 IEEE International Conference on, IEEE, pp 2034–2040
- 29. Lai R, Liang J, Zhao H (2013) A local mesh method for solving pdes on point clouds. Inverse Prob and Imaging 7(3):737–755
- 30. Levy B (2006) Laplace-beltrami eigenfunctions: Towards an algorithm that understands geometry. In: IEEE International Conference on Shape Modeling and Applications, invited talk
- 31. Litman R, Bronstein AM (2014) Learning spectral descriptors for deformable shape correspondence. IEEE transactions on pattern analysis and machine intelligence 36(1):171–180
- 32. Ovsjanikov M, Ben-Chen M, Solomon J, Butscher A, Guibas L (2012) Functional maps: a flexible representation of maps between shapes. ACM Transactions on Graphics (TOG) 31(4):30
- 33. Raviv D, Kimmel R (2014) Affine invariant non-rigid shape analysis. International Journal of Computer Vision
- 34. Raviv D, Bronstein AM, Bronstein MM, Kimmel R, Sochen N (2011) Affine-invariant diffusion geometry for the analysis of deformable 3d shapes. CVPR pp 2361–2367
- 35. Reuter M, Wolter FE, Peinecke N (2005) Laplace-spectra as fingerprints for shape matching. In: Proceedings of the 2005 ACM symposium on Solid and physical modeling, ACM, pp 101–106
- Reuter M, Wolter FE, Peinecke N (2006) Laplace-beltrami spectra as 'shape-dna' of surfaces and solids. Computer-Aided Design 38(4):342–366
- 37. Rodola E, Moeller M, Cremers D (2015) Point-wise map recovery and refinement from functional correspondence. arXiv preprint arXiv:150605603
- 38. Rustamov RM (2007) Laplace-beltrami eigenfunctions for deformation invariant shape representation. Eurographics Symposium on Geometry Processing
- 39. Shi Y, Lai R, Krishna S, Sicotte N, Dinov I, Toga AW (2008) Anisotropic Laplace-Beltrami eigenmaps: bridging Reeb graphs and skeletons. In: Computer Vision and Pattern Recognition Workshops, pp 1–7
- 40. Shi Y, Lai R, Gill R, Pelletier D, Mohr D, Sicotte N, Toga AW (2011) Conformal metric optimization on surface (cmos) for deformation and mapping in laplace-beltrami embedding space. In: International Conference on Medical Image Computing and Computer-Assisted Intervention, Springer, pp 327–334
- 41. Shi Y, Lai R, Toga AW (2013) Cortical surface reconstruction via unified reeb analysis of geometric and topological outliers in magnetic resonance images. IEEE transactions on medical imaging 32(3):511–530
- 42. Shi Y, Lai R, Wang DJ, Pelletier D, Mohr D, Sicotte N, Toga AW (2014) Metric optimization for surface analysis in the laplace-beltrami embedding space. IEEE transactions on medical imaging 33(7):1447–1463

43. Shtern A, Kimmel R (2015) Spectral gradient fields embedding for nonrigid shape matching. Computer Vision and Image Understanding 140:21–29

- 44. Shtern A, Sela M, Kimmel R (2016) Fast blended transformations for partial shape registration. Journal of Mathematical Imaging and Vision pp 1–16
- 45. Siddiqi K, Lauziere YB, Tannenbaum A, Zucker SW (1998) Area and length minimizing flows for shape segmentation. IEEE Transactions on Image Processing 7(3):433–443
- 46. Springborn B, Schröder P, Pinkall U (2008) Conformal equivalence of triangle meshes. ACM Transactions on Graphics (TOG) Proceedings of ACM SIGGRAPH 2008 27(3)
- 47. Sun J, Ovsjanikov M, Guibas L (2009) A concise and provably informative multi-scale signature based on heat diffusion. In: Computer graphics forum, Wiley Online Library, vol 28, pp 1383–1392
- 48. Tombari F, Salti S, Di Stefano L (2010) Unique signatures of histograms for local surface description. In: European conference on computer vision, Springer, pp 356–369
- 49. Vallet B, Levy B (2008) Spectral geometry processing with manifold harmonics. Computer Graphics Forum (Proceedings Eurographics)
- 50. Van Kaick O, Zhang H, Hamarneh G, Cohen-Or D (2011) A survey on shape correspondence. In: Computer Graphics Forum, Wiley Online Library, vol 30, pp 1681–1707
- 51. Vestner M, Lähner Z, Boyarski A, Litany O, Slossberg R, Remez T, Rodola E, Bronstein A, Bronstein M, Kimmel R, et al. (2017) Efficient deformable shape correspondence via kernel matching. In: 2017 International Conference on 3D Vision (3DV), IEEE, pp 517–526
- 52. Wang Y, Yin W, Zeng J (2015) Global convergence of admm in nonconvex nonsmooth optimization. arXiv preprint arXiv:151106324
- 53. Weiqiang Chen YY Jui JI (2016) An augmented lagrangian method for l1-regularized prolems with orthogonality constrains. SIAM Journal on Scientific Computing 38(7)
- 54. Wen Z, Yin W (2013) A feasible method for optimization with orthogonality constraints. Mathematical Programming 142(1-2):397–434